GeoScienceWorld
Lithosphere
Volume 2022, Article ID 4926735, 18 pages
https://doi.org/10.2113/2022/4926735

Lithosphere

Research Article

Energy Chaos Characteristic Evolution Analysis of Sandstones during Multilevel Unloading Subject to Different Confining Pressures

Shuang Dang,[1,2] Jing Bi,[1,2] Yu Zhao ,[1,2] Chaolin Wang,[1,2] Kaizong Xia,[3] and Fei Gan[1,2]

[1]*College of Civil Engineering, Guizhou University, Guiyang, Guizhou 550025, China*
[2]*Guizhou Provincial Key Laboratory of Rock and Soil Mechanics and Engineering Safety, Guizhou 550025, China*
[3]*State Key Laboratory of Geomechanics and Geotechnical Engineering, Institute of Rock and Soil Mechanics, Chinese Academy of Sciences, Wuhan, Hubei 430071, China*

Correspondence should be addressed to Yu Zhao; zytyut1@126.com

Received 21 June 2022; Accepted 2 August 2022; Published 5 September 2022

Academic Editor: Shaofeng Wang

In this study, multilevel and conventional unloading triaxial compression tests under different confining pressures are separately carried out to systematically reveal the deformation, energy evolution, and fracture characteristics of sandstone samples. Results show that under the multilevel unloading condition, the increase of the initial confining pressure has a more obvious inhibitory effect on the radial strain of sandstone, and the samples can fully exhibit elastic deformation and partial plastic deformation, showing obvious plastic characteristics. The radial energy growth factor is more sensitive than the axial energy growth factor during the process of confining pressure unloading, and the larger the initial confining pressure, the earlier the period-doubling bifurcation region and chaotic region are reached. To better understand the deformation and failure process of rock during engineering excavation, it is necessary to establish a constitutive relation describing the mechanical properties of rock. The three-step failure mode also proves that there are tensile and shear fractures in sandstone samples, in which the effects of tensile stress and shear stress are more or less interdependent in the failure process. It can be seen that multilevel unloading makes the energy conversion more adequate and reduces the sudden release of energy when the rock fails, reducing the possibility of rockburst and making the excavation unloading process safer. This will deepen the understanding of rock failure behavior and contribute to the better application of energy characteristics to relevant engineering practices.

1. Introduction

Rock is an important natural material that is widely encountered in various practical projects, especially underground construction, hydropower engineering, and mining engineering [1–6]. Many rock engineering studies prove that the rock steady-state stress field will change, and the fracture behavior is complex under the disturbance conditions such as excavation unloading action, fatigue loading action, explosion disturbance, and vibration action [7–11]. Therefore, it is significant to carry out the corresponding research on rock mechanics under unloading excavation conditions, to ensure the long-term stability of rock structures [12–15].

In geotechnical engineering, the rock will be disturbed by various unloading actions, resulting in certain damage and even failure. Different stress paths have various impacts on the mechanical characteristics [16–20], energy evolution [21, 22], and fracture mechanism of rocks [23, 24], and many scholars have conducted research in this area. For example, in the application, Gong et al. [25] investigated the linear energy storage and dissipation laws of rock materials under uniaxial compression. Lei et al. [26] revealed the relationships among the mechanical characteristics, failure modes, and energy storage properties of sandstone, and the constitutive equations of uniaxial compression samples are obtained. Peng et al. [27] researched the deformation

characteristics of sandstones during cyclic loading and unloading under different confining pressures.

We know the effect of the cyclic loads is mainly reflected in the antifatigue performance of rock [28–32], while in practical engineering, the failure of rock has mainly resulted in the increase of deviational stress under unloading action [33–35]. Therefore, numerous studies have been carried out on rock fracture behavior under reducing confining pressures conditions [36–38]. Feng et al. [39] concluded that the bearing capacity and deformation of the unloading stress path were greater than those of the loading stress path. Ding et al. [40] demonstrated that the sample deformed in a more obvious ductile failure manner at higher confining pressure, whereas in the unloading confining pressure experiments, brittle failure was more obvious. Zhao et al. [41] explored the characteristics of energy evolution of sandstone subject to confining pressure unloading conditions. Zhang et al. [42] pointed out the evolution and transformation of strain energy under triaxial unloading confining pressure conditions.

The above research is aimed at the linear unloading or cyclic unloading process of confining pressure, while the stress multilevel unloading process in practical engineering, especially high slope and deep mining project excavation, is more widely applied [43, 44]. On the basis of the above discussion, rock failure is substantially the result of the continuous transformation of energy in the object and the outside world. Rock deformation and failure subject to the multilevel unloading confining pressure can be analyzed in terms of energy nonlinear evolution. Energy evolution chaotic characteristic is a common property of rock systems when they are destabilized, and the chaotic state is unstable and irreversible [45–47]. The stage of rock deformation and failure can be basically determined by using the energy iterative growth factor, and the degree of rock deformation and failure can be dynamically analyzed through the energy evolution curve, which can timely and intuitively monitor the rock stability and effectively avoid the occurrence of disasters.

In view of the widespread application of the grading unloading method in actual construction, the real-time energy nonlinearity evolution of the whole process of deformation and failure during the multilevel unloading confining pressure process has been rarely investigated. In this paper, the energy nonlinear chaotic characteristics of the multilevel unloading method are studied, the constitutive equations are tried to be established, and the failure mechanism is analyzed [48–53]. Meanwhile, it is compared with the conventional unloading method under the same stress condition. The dynamic multilevel unloading of simulating excavate rock engineering is realized, which has certain guiding significance for the monitoring and early warning of construction safety.

2. Experimental Materials and Procedures

2.1. Sample Preparation. This paper takes the shallow yellow coarse sandstone in the Jiangsu area as the test sample. A standard cylindrical sandstone sample of 50 mm × 100 mm (diameter × length) was prepared to evaluate its deformation evolution characteristics under different unloading paths. These samples are divided into 3 groups. The first group (2 samples in a group) is marked as the uniaxial compression tests group, named U1 and U2. The secondary group is marked as a triaxial multilevel unloading test group (4 samples in a group). Samples are named TA-1, TA-2, TA-3, and TA-4. The last one is marked as a linear unloading group (4 samples in a group). Samples are named TB-1, TB-2, TB-3, and TB-4.

2.2. Experimental Program. To reflect the real environment under unloading excavation conditions, the samples TA-1, TA-2, TA-3, and TA-4 are used for conducting the multilevel decreasing confining pressure with constant axial stress. Samples TB-1, TB-2, TB-3, and TB-4 are used for conducting triaxial unloading tests with the linear decreasing confining pressure and constant axial stress.

The stress paths of the above three tests are recorded as stress paths 1, 2, and 3 (as shown in Figure 1). Stress path 1 is the conventional uniaxial loading to test the uniaxial compression strength of sandstone samples. Moreover, for the stress paths 2 and 3, the maximum confining pressures are set as 10 MPa, 20 MPa, 30 MPa, and 40 MPa, respectively. The stresses are decreased by 1/10 initial confining pressure at each level. Furthermore, each level is completed in 60 seconds. In the compression loading stage, the confining pressure and the axial stress are loaded at the same time to prevent the sandstone sample from being crushed. Then, the confining pressure and the initial stress remain constant for 5 min to ensure the complete vertical load. The value of 50 MPa of axial stress is set to prevent the samples to be destructive after confining pressure unloading resulting in the increasing strength of samples after compaction. In addition, the testing process is controlled and executed automatically after the programming is completed. The confining pressure is conducted in accordance with stress paths 2 and 3 until the rock samples fail.

2.3. Test Equipment. As shown in Figure 2, the servo-controlled material triaxial test system DSZ-1000 (multi-field-coupled rock mechanics testing machine) is used in this study in the Guizhou University. The maximum axial loading is 1000 kN. The maximum confining pressure is 60 MPa. The effective stiffness of the main engine is up to 5 GN/m to ensure the test accuracy. The deformation of the axial and radial strain sensor (Epsilon Electronic Extensor) is measured and converted into a signal and imported into the automatic strain calculation program. During the test, the axial and radial is a constant loading rate up to stress to meet the setting value. Through the complete program of the test equipment, the stress, strain, and confining pressure of the sample are recorded and calculated in real-time.

2.4. Energy Conversation Mechanism. Both axial stress and confining pressure have positive effects on sandstone samples subject to unloading conditions. With the increase of σ_1, the energy input of the sample increases until the

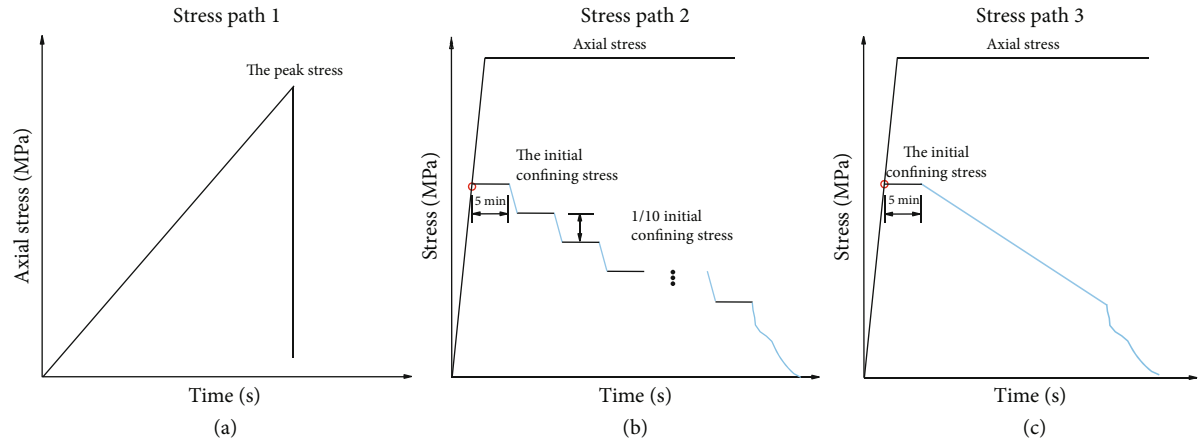

Figure 1: Loading and unloading stress paths: (a) stress path 1: uniaxial compression test, (b) stress path 2: multilevel triaxial unloading test, and (c) stress path 3: linear triaxial unloading test.

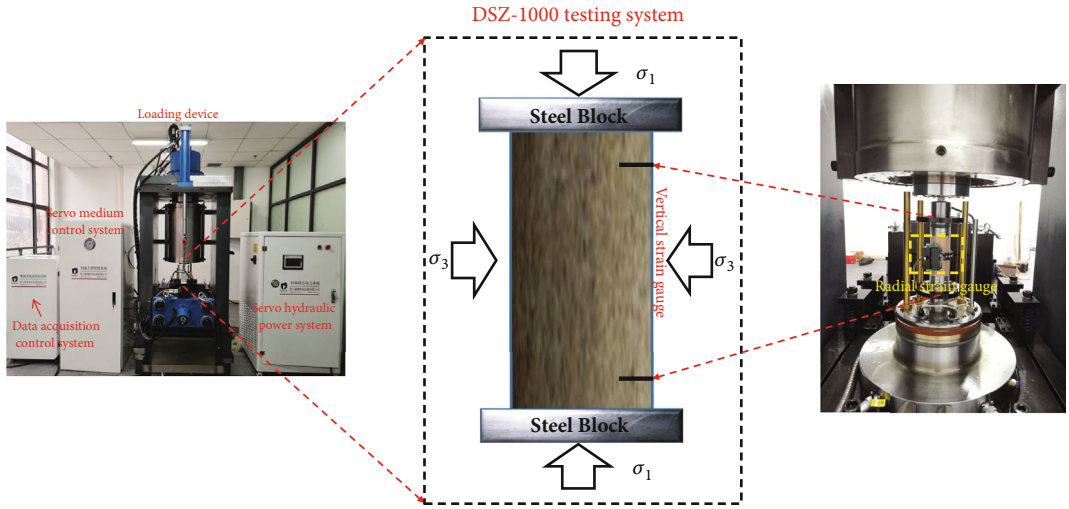

Figure 2: Test devices.

maximum deviatoric stress (σ_1-σ_3) is obtained. In the process of sample deformation, negative work is done by confining pressure due to the radial expansion of the sample. Therefore, the strain energy of the triaxial unloading test can be presented as [22, 37]:

$$U = U_1 + U_3 + U_0, \tag{1}$$

where U_1 is the axial total energy of the sample due to the axial stress, U_3 is the radial total energy of the sample due to the confining pressure, and U_0 is the absorbed strain energy.

By integrating the stress-strain curve, the absorbed and consumed strain energy (U_1 and U_3) at any time during the test can be obtained [22, 37]:

$$\begin{aligned} U_1 &= \int_0^{\varepsilon_1^t} \sigma_1 d\varepsilon_1, \\ U_3 &= 2\int_0^{\varepsilon_3^t} \sigma_3 d\varepsilon_3, \end{aligned} \tag{2}$$

where ε_1^t and ε_3^t are the axial strain and radial strain at any loading time t, respectively. The integrals in Equations (3) and (4) can be achieved by accumulating the area of the trapezoid in the stress-strain curve, demonstrated in Figure 3.

$$U_1 = \sum_{i=1}^{n} \frac{1}{2}\left(\sigma_1^i + \sigma_1^{i+1}\right)\left(\varepsilon_1^{i+1} - \varepsilon_1^i\right), \tag{3}$$

$$U_3 = \sum_{i=1}^{n} \frac{1}{2}\left(\sigma_3^i + \sigma_3^{i+1}\right)\left(\varepsilon_3^{i+1} - \varepsilon_3^i\right), \tag{4}$$

where n is the total number of trapezoids in the stress-strain curve and i is the transition points.

According to the principle that the total energy of the rock remains unchanged, in the whole test, if there is no heat transfer with the outside world in any physical process, the total energy is equal to the sum of the external force of the total load on the rock sample. The dissipated

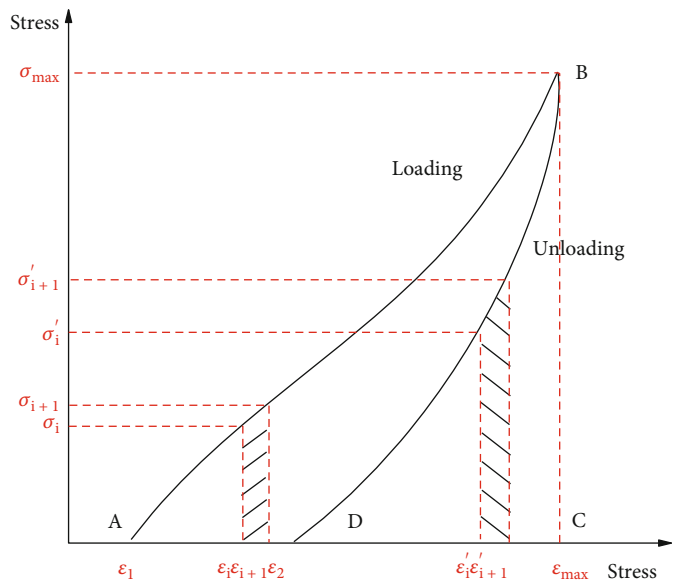

Figure 3: Schematic diagram for calculation of strain energy.

energy and the elastic energy of the rock satisfy the following equation [22, 37]:

$$U = U_e + U_d. \tag{5}$$

The elastic strain energy U_e at any time under the conventional triaxial compression can be obtained according to the studies [22, 37].

$$\int udV = \int u_e dV + \int u_d dV, \tag{6}$$

where u represents the total energy density, u_e indicates the elastic energy density, u_d denotes the dissipated energy density, and V indicates the volumetric of rocks.

3. Characteristics of Stress-Strain Curves under Different Stress Paths

The complete stress-strain curve of the sandstone sample in the uniaxial compression test is plotted in Figure 4. It shows the properties of four stages (the densification, elasticity, yielding, and failure procedures). Under the uniaxial compression condition, the stress quickly declines after it reaches the peak stress showing obvious brittleness characteristics. From the test results, the average uniaxial compressive strength of about 34.65 MPa and Young's modulus of about 2.85 GPa can be obtained.

For the sandstone samples experiencing the loading and unloading stages, the axial, radial, and volumetric stress-strain curves are illustrated in Figure 5. On the whole, under stress path 2 and stress path 3, the whole evolution trend of strain has a strong consistency.

In stress path 2, the axial strain grows stepwise, while the radial strain and volumetric strain decrease stepwise. Then, the deformation increment increases gradually with the unloading progress. All of these show a characteristic of steeper steps. Under initial unloading, the axial strain value of sample TA-1 is 0.01057, while sample TA-4 is 0.00702, a reduction of 44%. The initial value of radial strain is about zero for samples TA-1 and TA-2. The radial strain increases with the initial confining pressure. The initial value of radial strain is 0.000794 and 0.003857 for samples TA-3 and TA-4, respectively. During the whole experiment, the volumetric strain is almost greater than zero, and the sample does not expand until the failure of the samples due to the combined action of axial stress and confining pressure.

The microcracks of rock are closed under external force consistent with the compaction stage of rock. The curve shows that the axial strain parallels with the abscissa, demonstrating that the rock is in the elastic phase. In the cycles of the last few levels, the strain increases slowly with the stress. At this time, the samples gradually transform to the plastic stage when the strain incremental grows significantly. Then, the irreversible deformation suddenly increases, and the samples fail in the last level.

In stress path 3, the strains increase (decrease) gradually in the early unloading process, while in the final stage of unloading, the strains show a sharp increase (decrease) trend. The changes in other aspects are basically consistent with stress path 2.

4. Conversion of Strain Energy during Sandstone Sample Failure

4.1. Energy Evolution under Different Triaxial Unloading Conditions. Evolution curves are drawn with running time as abscissa and axial strain energy as ordinate, as presented in Figure 6. Although the initial confining pressures of each sample are different, the overall variation trend of curves is basically the same. Axial strain energy curves present an increase trending in the whole unloading process.

Figure 6(a) shows a strong consistency in the axial energy evolution curve. The initial axial strain energy decreases with

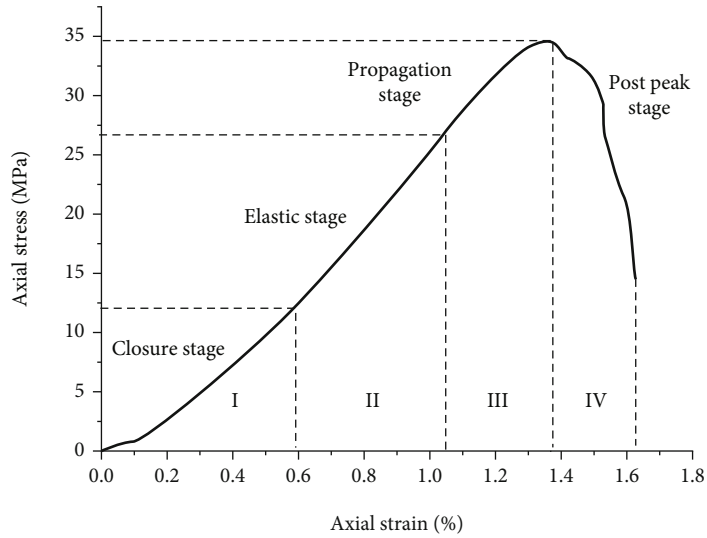

Figure 4: Complete stress-strain curves of rock samples in the uniaxial compression tests.

the increase of initial confining pressure. At the initial level of unloading, the axial strain energy on the samples of TA-1~TA-4 is 0.2278 MJ/m^3, 0.2068 MJ/m^3, 0.1821 MJ/m^3, and 0.1300 MJ/m^3, respectively. The axial strain energy of the sample TA-4 is only 57% of that of the sample TA-1. The axial strain energy of the samples TA-1~TA-3 increase synchronously with the same amplitude, and the curves are approximately parallel. However, the axial strain energy of sample TA-4 decreases first and then increases, and the strain energy decreases by 40% compared with sample TA-1. The consequences of the increase in confining pressure convert more energy into radial strain energy. This phenomenon can be confirmed in Figure 7(a). Nevertheless, with the unloading process, the samples of the axial strain energy increase gradually in the previous levels and a more obvious increment in the last few levels.

Figure 6(b) is the axial strain energy evolution curve of stress path 3. The initial axial strain energy decreases with the increase of initial confining pressure. Relative to path 2, the initial values of axial strain energy of path 3 are not much different, the energy curves of samples TB-1~TB-3 are nearly parallel, and the energy growth is basically synchronized. At about 3000 seconds, the energy increases rapidly, and the confining pressure corresponds to 2.1647 MPa, 4.3206 MPa, and 6.5576 MPa, which is basically about 80% of the initial confining pressure. For sample TB-4, the axial strain energy curve lies above the other curves when the initial confining pressure is unloaded to 23.4388 MPa. This is quite different from the axial strain energy curve corresponding to the same confining pressure of stress path 2. At this time, crack coalescence develops rapidly, which is reflected in the rapid accumulation and release of energy. Different paths and confining pressures will affect the magnitude and evolution laws of axial strain energy.

Except for confining pressure of 40 MPa conditions, the axial strain energy of path 3 is smaller than that of path 2. The curve under higher confining pressure has different characteristics from those under other lower confining pressure conditions, and the accumulation and release of axial strain energy are different. The difference between stress paths 2 and 3 in the unloading process is that path 2 belongs to multilevel unloading. The confining pressure decreases by 1/10 of the initial confining pressure step by step, and the strain increases gradually at first when the axial stress remains unchanged, but the strain increases more obviously in the later level of unloading. Stress path 3 is continuous unloading of the confining pressure, during which the strain continues to grow, and the axial strain energy increases slowly at first, but increases rapidly in the middle and later levels of unloading, especially for the sample TB-4.

Overall, it seems that the axial strain energy of path 2 is larger than that of path 3 under the confining pressure conditions of 10 MPa, 20 MPa, and 30 MPa. The axial strain energy of path 3 is higher than that of path 2 under the confining pressure conditions of 40 MPa. At the same time, it can be seen that under the condition of path 2, gradually increasing step by step, except for the few last levels, the ahead levels are basically horizontal. This is because the strain is not further increased, and the axial strain energy incensement is small. However, at the last level, the confining pressure value is low, and the cracks of the internal sample increase rapidly to extend and penetrate until the sample fails, and the elastic energy stored in the rock is released rapidly.

It is worth pointing out that on higher confining pressure, the axial strain energy increase in the last level is less obvious, reflecting the small increase of axial strain. It also confirms that the confining pressure inhibits the destruction of the rock, and more energy is required for the destruction of the rock under higher confining pressure conditions. In stress path 2, the curves of sample TA-4 all appear a longer section of the horizontal segment, which also indicates that the axial strain remains basically unchanged when the rock is initially unloaded under the high confining pressure condition, indicating that the rock has a more elastic reserve and stronger ability to resist failure. In path 3, a small horizontal

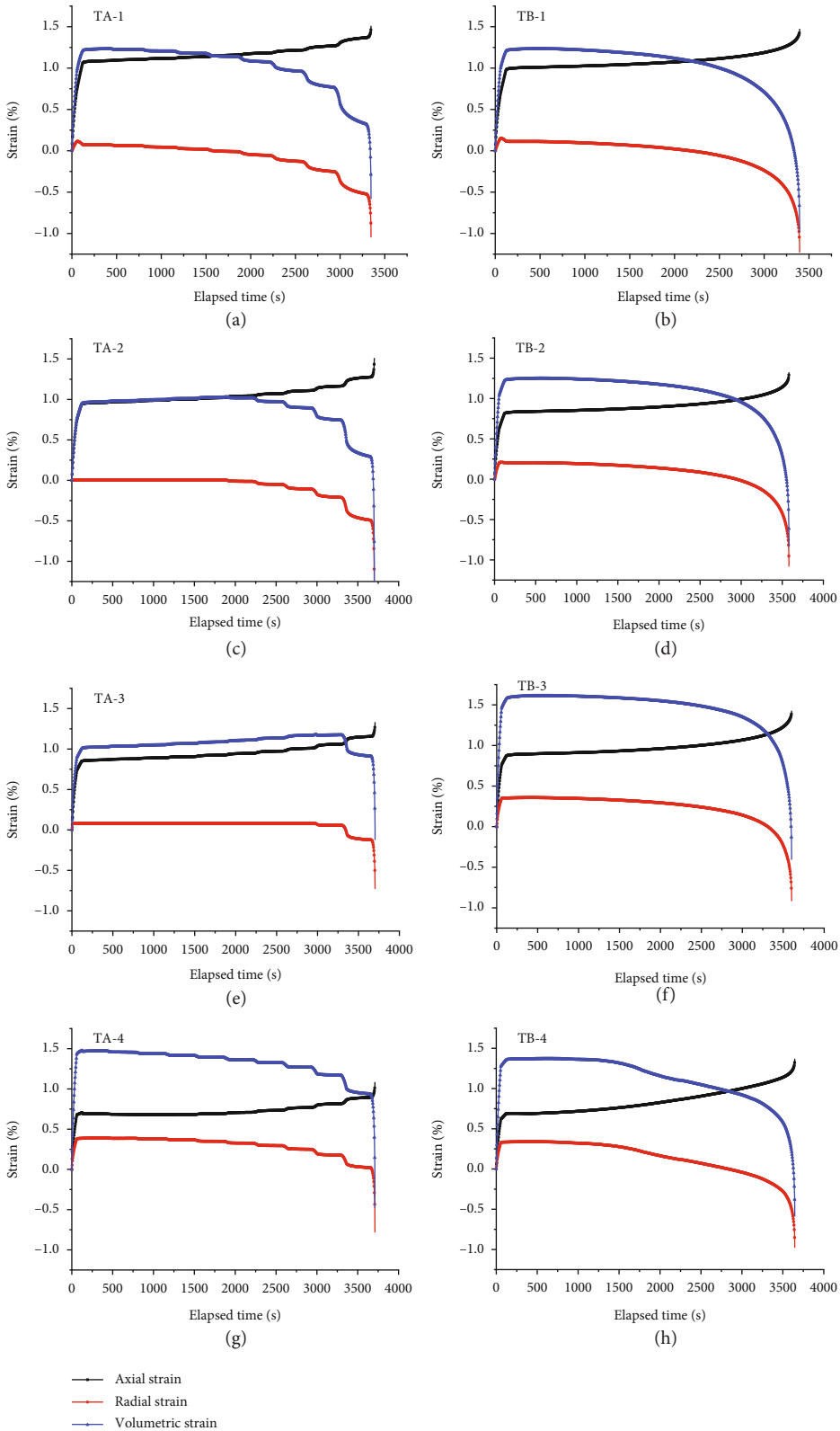

FIGURE 5: Curves of the axial, radial, and volumetric strain under stress paths 2 and 3: (a), (c), (e), and (g) represent the samples of TA-1~TA-4 in stress path 2, and (b), (d), (f), and (h) represent the samples of TB-1~TB-4 in stress path 3.

section appears in the curve, there is no increase in axial strain energy at this time. After that, the curve increases more significantly than other confining pressure conditions, forming a greater contrast with stress path 2, which can indicate that multilevel unloading has a suppressive effect on axial deformation and energy dissipation. Especially in

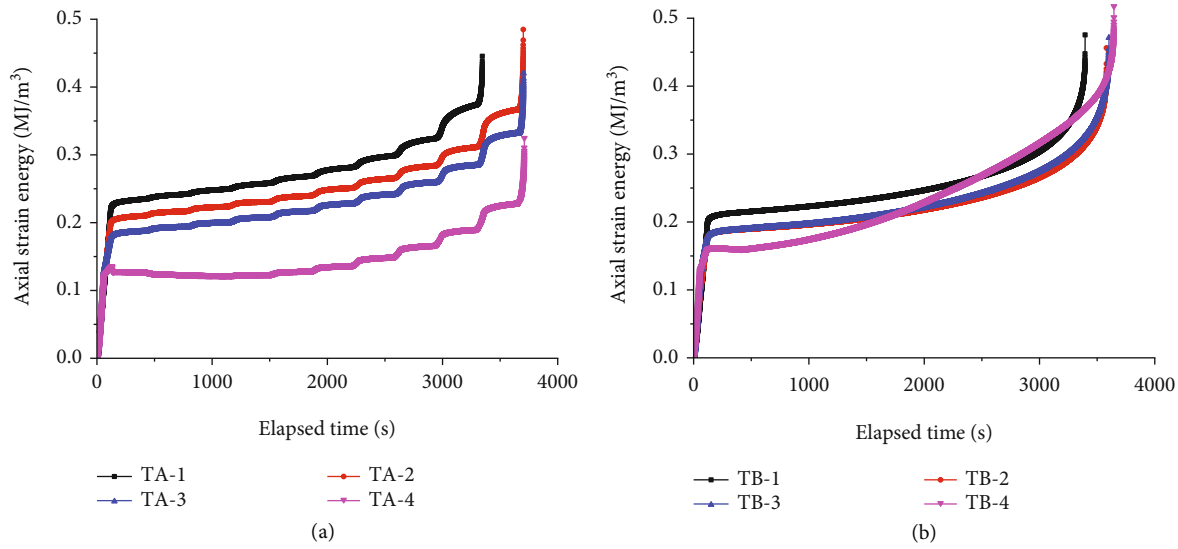

Figure 6: Axial strain energy evolution curves under stress path 2 and 3: (a) stress path 2, (b) stress path 3.

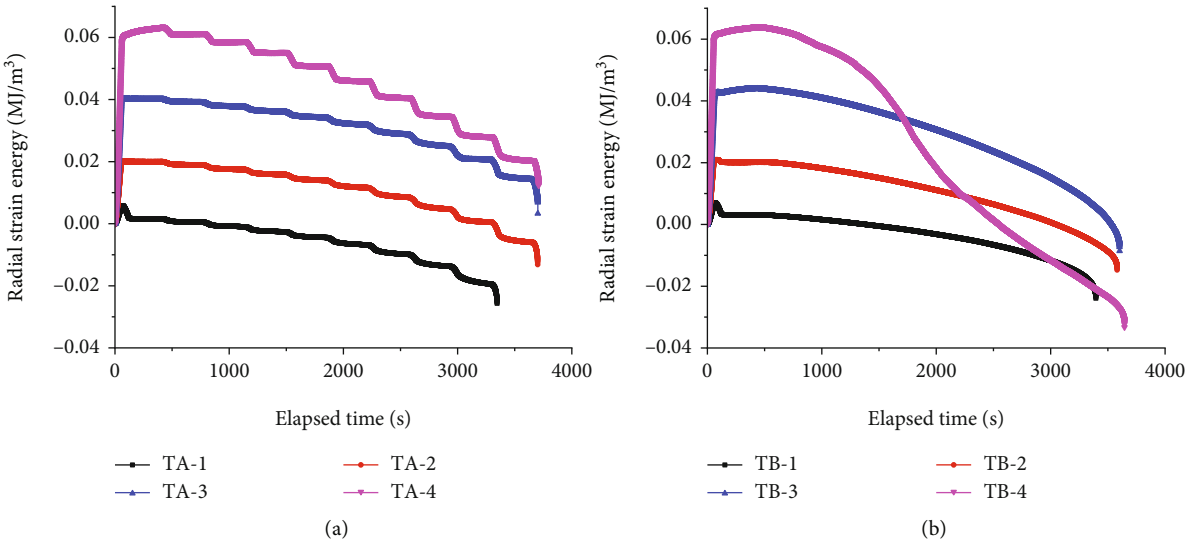

Figure 7: Radial strain energy evolution curves under stress paths 2 and 3: (a) stress path 2, (b) stress path 3.

higher confining pressure excavation unloading conditions, multilevel unloading is a safer unloading method.

Figure 7(a) is the radial strain energy evolution curve of different confining pressures under stress path 2 showing a strong consistency. The initial axial strain energy increases with the initial confining pressure. The initial value of radial strain energy of the TA-1~TA-4 samples in the unloading stage is 0.0018 MJ/m^3, 0.0200 MJ/m^3, 0.0406 MJ/m^3, and 0.0609 MJ/m^3, severally. The radial strain energy decreases stepwise, and the decreased amplitude difference becomes larger and larger during the unloading process. When the samples fail, the radial strain energy are -0.025 MJ/m^3, -0.01317 MJ/m^3, 0.00328 MJ/m^3, and 0.0122 MJ/m^3, respectively. The sample TA-4 with confining pressure of 40 MPa has the largest decrease in radial strain energy, and the reduced strain energy of each level is also larger than that of other samples, and the other curves are approximately parallel.

Figure 7(b) is the radial strain energy evolution curve of different confining pressures under stress path 3. The initial value of radial strain energy of the TB-1~TB-4 samples in the unloading stage is 0.0031 MJ/m^3, 0.0201 MJ/m^3, 0.0426 MJ/m^3, and 0.0619 MJ/m^3, severally. The curve is maintained at this energy level during a subsequent period. After unloading, the radial strain energy decreases gradually, and the slope increases. At about 3000 seconds, the slope increases sharply. When the samples fail, the radial strain energy are -0.023 MJ/m^3, -0.014 MJ/m^3, -0.008 MJ/m^3, and -0.033 MJ/m^3, respectively. However, the radial strain energy of the sample TB-4 decreased by a large margin, resulting in an energy drop (0.0949 MJ/m^3). The curve of sample TB-4 intersects with the other three curves, and when

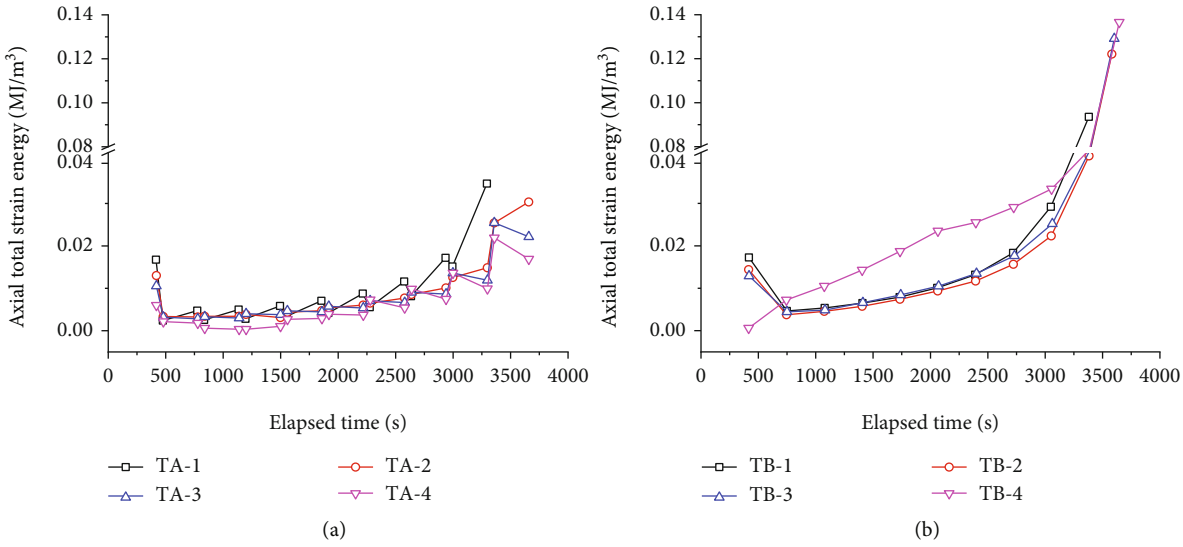

Figure 8: Each level of axial total strain energy curves under stress paths 2 and 3: (a) stress path 2, (b) stress path 3.

the rock fails, the radial strain energy reaches the maximum value.

Compared with stress paths 2 and 3, except for the confining pressure of 40 MPa, the initial and ultimately radial strain energy of the unloading under the two paths is basically the same. However, the radial strain energy of the samples TA-4 and TB-4 is quite different. It manifests that the stress path has a great impact on the radial strain energy under high confining pressure conditions. At this time, the cracks inside the sample rapidly increase and penetrate until the sample fails, and the energy stored in the rock is rapidly released. It indicates that multilevel unloading has the same inhibitory effect on the radial strain development and energy dissipation, which is consistent with the phenomenon in Figure 6(b).

4.2. Energy Evolution Laws with Different Confining Pressures. Figure 8(a) is the axial total strain energy evolution curves under stress path 2 on each level. During the unloading process, the initial and failure values of the axial total strain energy of each unloading level decrease with the increase of confining pressure. The axial strain energy increases in turn and the amplitude increases gradually in the whole unloading process. The axial strain energy of sample TA-1 decreases in the unloading section (confining pressure decrease), increases in the platform section (confining pressure remain stable), and reaches the maximum when the sample fracture. The axial strain energy of sample TA-2 in the unloading section and platform section is basically the same in the first few levels. By about 3000 seconds, the unloading section has a differential growth and the increased amplitude is higher than that of the platform section. The axial strain energy of the samples TA-3 and TA-4 in the unloading section and platform section is a little different at the beginning, but the platform section has a downward trend. In the last few levels, the axial strain energy of the unloading section increases rapidly; meanwhile, the platform section decrements largely.

Figure 8(b) demonstrates the values obtained when the confining pressure decreases to the corresponding value of path 2 under the action of path 3. The curve shows a downward and then upward trending, and the increased amplitude is the largest one in the last level of unloading. The curves of samples TB-1~TB-3 basically coincides, but the curve of sample TB-4 is significantly higher than the other three curves and reaches the maximum value when the sample fails.

From the perspective of the axial total strain energy value, the energy of the unloading path 3 is generally higher than that of path 2. Particularly, at the time of rock failure, the energy released by path 3 is much higher than that of path 2, and the higher the initial confining pressure, the larger the energy released. This is because the axial strain increases continuously during the linear unloading conditions, the irrecoverable deformation accumulates gradually, and the continuously increasing deviatoric stress makes the energy stored in rock in the form of elastic energy until the confining pressure gradually decreases to a smaller value, the energy is suddenly released, and the rock fails.

The confining pressure has a certain inhibitory effect on the development of the strain, and the unloading of the confining pressure leads to an increase in the deviatoric stress. Usually, at the initial stage of unloading, the rock is in the linear elastic stage, the axial strain accumulates, and the axial strain energy grows linearly. At the later stage of unloading, the irrecoverable strain increases rapidly, and the axial strain energy increases sharply until the rock fails.

However, in the case of high confining pressure, such as TA-3 and TA-4 samples, the axial strain energy increases in the unloading section, while the axial strain energy decreases in the platform section. The deviatoric stress intermittently increases the samples which can fully demonstrate the elastic deformation and partial plastic deformation; the axial strain has a certain recovery, but with the continuous unloading, the deviatoric stress gradually increases, the irrecoverable

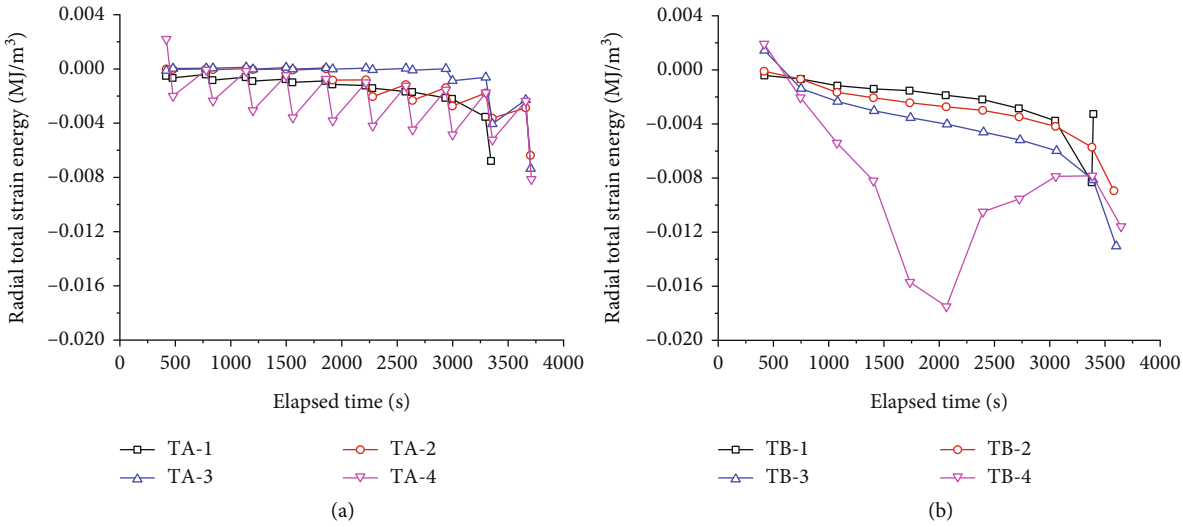

Figure 9: Each level of radial total strain energy curves under stress paths 2 and 3: (a) stress path 2, (b) stress path 3.

strain rapidly increases, and the higher the confining pressure, the more obvious the plastic characteristics.

Figure 9(a) is the radial total strain energy evolution curve of stress path 2. The initial value and failure value of radial strain energy increase with confining pressure. From the view of the radial total strain energy, the energy values of the unloading path 3 are generally higher than that of path 2. In particular, the energy released by path 3 is much higher than that of path 2 at the initial confining pressures of 30 MPa and 40 MPa at the time of sample failure.

Under the action of path 2, except for the confining pressure of 40 MPa, the radial total strain energy of other samples has a long horizontal section, and the energy value of this horizontal section is almost zero, indicating that it is almost no energy dissipation in the process, and the strain energy absorbed by the rock is almost stored as elastic energy. In the last few levels of unloading, the energy accelerates growth. Under the confining pressure of 40 MPa, from the curve, there is a certain degree of energy drop in the unloading process at each level, but after a short period of confining pressure stabilization, there is a certain rebound of energy, but the overall dissipation energy increases. It can be seen that the multilevel unloading method provides a certain buffer and recovery period for the rock.

For stress path 3, the energy increases steadily under the continuous unloading conditions; the dissipated energy increases gradually. The strain does not recover in time during the gradual increase of the deviatoric stress, the crack continues to expand, and more energy is released, resulting in sample failure. The radial total strain energy of the sample TB-4 shows a trend of first increasing and then decreasing. This is due to the fact that sandstone belongs to sedimentary rocks containing certain pores and fissures, and there may be more pores in this sample. In the process of continuous reduction of the confining pressure, the deviatoric stress increases, the sample is continuously compacted, the pores are further closed, the strain increases, and the strain energy gradually increases. However, after the pores are compacted and closed, the action of the confining pressure increases the normal stress on the fracture surface inside the rock, which makes the deformation of the rock sample require a larger load effect. At this time, the strain no longer continues to increase, and the strain energy is recovered to a certain extent. Until the final stage, the propagation of the crack leads to the increase of the irrecoverable strain, the strain energy is rapidly increased and released, and the rock sample is fractured.

5. Discussion

5.1. Chaos Theory and Logistic System. Chaos theory is a science established in the 1960s. It is an evolutionary theory that the system suddenly changes from an ordered state to a disordered state. It is a discussion of the way and mechanism of the formation of the internal random process in the deterministic system. Chaos refers to the erraticism or irregularity in deterministic systems, which is a universal property of a system when it is unstable. The chaotic characteristics of disasters are mainly manifested in the short-term predictable but long-term unpredictable characteristics. The evolution of the disaster system is studied and predicted by the Lyapunov index, Kolmogorov descendant, and fractional dimension, which achieves the purpose of disaster prevention.

For deterministic nonlinear systems, whether it is mathematically defined chaos associated with infinite processes or physical chaos under finiteness defined according to the actual observable data, as long as it has three essential characteristics of "bounded," "aperiodic," and "sensitive initial conditions," then the system can be considered as chaotic. A logistic system is a simple chaotic system [45].

Power system

$$\frac{dx}{dt} = f(x, \mu) = \mu x(1 - x). \tag{7}$$

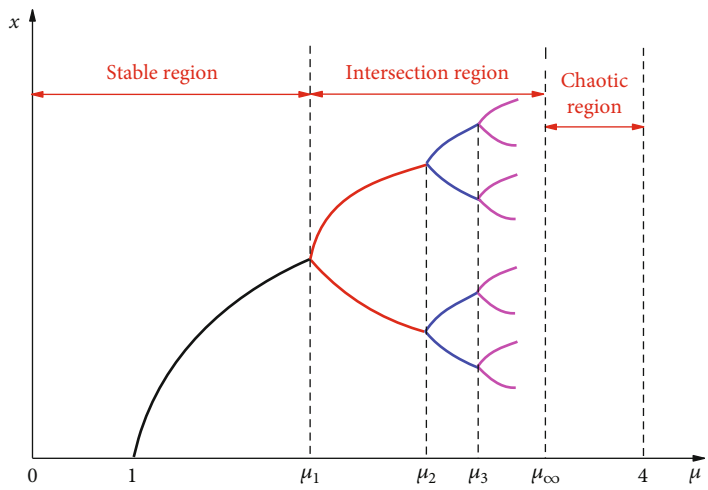

Figure 10: Illustration of the logistic equation (not to scale).

Discrete continuous-time to obtain differential form

$$x_{n+1} = f(x_n, \mu) = \mu x_n(1 - x_n), \quad n = 1, 2, \cdots, \tag{8}$$

where x_n is the state at time t_n, x_{n+1} is the state at time t_{n+1}, and they are time series. μ is a dimensionless system parameter.

Figure 10 is a logistic equation solution diagram. It can be seen that the properties of its solution depend deeply on the parameters μ, which are divided into stable region, double periodic bifurcation region, and chaotic region.

5.1.1. Stable Region. At $\mu \le \mu_1 = 3$, the system is in a stable region, and the iterative result is a definite value independent of the initial conditions.

5.1.2. Double Periodic Bifurcation Region. At $3 = \mu_1 < \mu \le \mu_\infty \approx 3.5699$, the system is in a period-doubling bifurcation state; at $\mu > 3$, the iterative results are uncertain. The system solution appears alternately around two points. When $\mu > \mu_2 \approx 3.4495$, the 2-point period becomes a 4-point period. When $\mu > \mu_3 \approx 3.5441$, the 4-point period becomes unstable and comes into the 8-point cycle. This bifurcation phenomenon with period-doubling of 1 minute 2, 2 minutes 4, and 4 minutes 8 is bifurcation with period-doubling. The bifurcation points are shown in Table 1.

5.1.3. Chaos Region. The spacing between the adjacent bifurcation points becomes smaller and smaller during the doubling period crossover. The μ value increases slightly, and the period will double until $\mu = \mu_\infty \approx 3.5699$. Then, the system comes into an infinite period, that is, a chaotic state.

5.2. Bifurcation and Chaos Characteristics. Equation (9) is a generalized logistic equation. To further study the nonlinear characteristics of rock energy evolution during the loading process, the evolution sequence of energy density values with

Table 1: Values of parameters at bifurcations.

Bifurcation situation	μ
1⟶2	3
2⟶4	3.449487743
4⟶8	3.544090359
8⟶16	3.564407266
16⟶32	3.568759420
⋮	⋮
Bifurcation→chaos	3.569945672

axial stress is investigated. The energy evolution is written in the form of a wormhole equation:

$$u_i = \frac{k}{1 + e^{-r\sigma - kc}}, \tag{9}$$

$$u_i^{j+1} = \mu u_i^j \left(\frac{1 - u_i^j}{k}\right), \tag{10}$$

where u_i^j is the energy density value at a certain stress level σ_j, u_i^{j+1} is the energy density value at the stress level $\sigma_{j+1} = \sigma_j + \Delta\sigma$, μ is the energy iterative growth factor, which represents the iterative growth effect of energy during loading, a function of axial stress σ, and k is the maximum value of energy u_i.

Order

$$\eta_i^j = \frac{u_i^j}{k}. \tag{11}$$

Equation (10) can be expressed as:

$$\eta_i^{j+1} = \mu \eta_i^j \left(1 - \eta_i^j\right). \tag{12}$$

Equation (12) is a standard logistic mapping, $\eta_i^j \in [0, 1]$, $\eta_i^{j+1} \in [0, 1]$, and $\mu \in [0, 4]$.

Figure 11 shows the whole process of the rock being compressed by external forces; with the increasing stress, the state of the rock can be roughly divided into the compaction stage, elastic stage, and plastic stage [36, 54, 55].

From the perspective of energy nonlinear evolution, the whole process of rock deformation and failure can be divided into the following four stages:

(1) $\mu \in (0, 1]$. The rock mass system is in a state of attenuation or calm (stage I in Figure 11); there is almost no microfracture activity when the sample is subjected to artificial unloading or natural relaxation

(2) $\mu \in (1, 3]$. The rock is in the stage of microfracture compaction and elastic deformation (stage II in Figure 11). The energy is continuously input, and most of it can be accumulated in the rock mass; the energy equilibrium state is gradually stabilized. The internal microfracture activity gradually becomes active, and oscillatory change occurs driven by energy

(3) $\mu \in (3, 3.5699]$. When the rock enters the stage of fracture development and propagation (stage III in Figure 11), the internal structure of the rock begins to change significantly. The convergence of macroscopic crack propagation reduces the energy storage capacity of the rock mass. The microfracture activity shows complex periodic rhythm in time and orderly self-organizing structure in space

(4) $\mu \in (3.5699, 4]$. The rock system enters the stage of unstable development and failure (stage IV in Figure 11). The macroscopic main crack begins to pass through; the spatial structure changes irregularly with time at every time in space. The energy dissipated increases sharply, and the energy equilibrium state gradually loses stability. The system will be irreversibly unstable when receiving the disturbance. These four stages represent the dominant stage of energy attenuation, energy accumulation, energy dissipation, and energy release in the rock

The variation curve of parameter μ with the increase of axial stress can be calculated by Equation (12). As shown in Figure 12, under the different confining pressures, the variation law of μ is basically the same. With the monotonic increase of stress, the initial stage of loading increases slowly and then increases faster and faster. Its value changes from the initial $\mu = 1$ to the peak stage value of $\mu \approx 4$, that is, the system changes from the stable region to the double bifurcation region and then to the chaotic region.

The trend of the curve of stress path 2 is basically the same; the slope of the curve is changing from small to large. When the deviatoric stress increases to 96.83% of the peak strength and μ increases to the critical value of 3.00, the fixed point is unstable and enters the period-doubling bifurcation region. As the stress increases, the bifurcation process accelerates. When the deviatoric stress increases to 97.40% of the peak stress, the value of μ increases to the critical value of 3.5699. The double period bifurcation process ends, and the system enters a chaotic state. The stress value slightly increases, and the value of μ increases linearly. From the stable crack growth stage to the stage of crack instability propagation, the rock presents the characteristics of brittle failure. For stress path 3, the trend of the curve is similar to stress path 2. However, when the confining pressure is 40 MPa, the curve is relatively gentle, and the rock presents certain plastic characteristics.

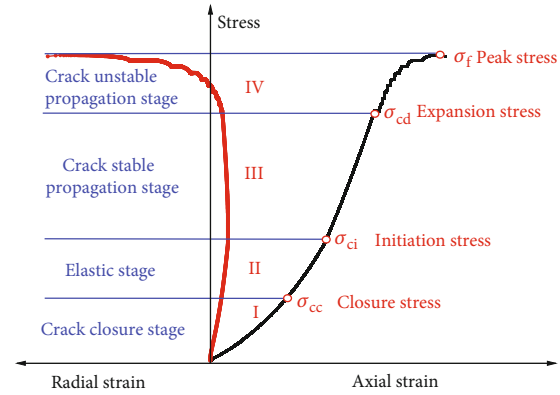

Figure 11: Division of four stages in typical triaxial compression state.

From Figures 12(c)–12(f), under the same confining pressure of different paths: for the confining pressure of 10 MPa, path 2 reaches the period-doubling bifurcation region and chaotic region earlier than path 3. For the confining pressure of 20 MPa and 30 MPa, path 2 and path 3 almost simultaneously reach the same axial energy growth factor. Path 3 reaches the period-doubling bifurcation region and chaotic region earlier than path 2 under the confining pressure of 40 MPa.

Figures 12(a) and 12(b) present that the larger the initial confining pressure, the earlier the period-doubling bifurcation region and chaotic region is reached, and the axial energy growth factor in the final level of unloading gradually becomes slower from the steep increase. Under the condition of path 2, the 9th level of TA-1 enters the period-doubling bifurcation region, and the 10th level enters the period-doubling bifurcation region under other confining pressure conditions. Given the above discussion, multilevel unloading mode has a certain inhibitory effect on energy growth.

Figure 13 for stress path 2, the period-doubling bifurcation area of the system begins to appear with confining pressures of 1.9924 MPa, 1.9937 MPa, 5.2909 MPa, and 7.9998 MPa, respectively. When the system enters into a chaotic state, the confining pressures are 1.9924 MPa, 1.9937 MPa, 4.2889 MPa, and 6.2473 MPa, respectively. For stress path 3, the period-doubling bifurcation area of the system begins to appear with confining pressures of 1.5311 MPa, 2.9265 MPa, 3.9945 MPa, and 8.4524 MPa, respectively. When the confining pressures are 1.3296 MPa,

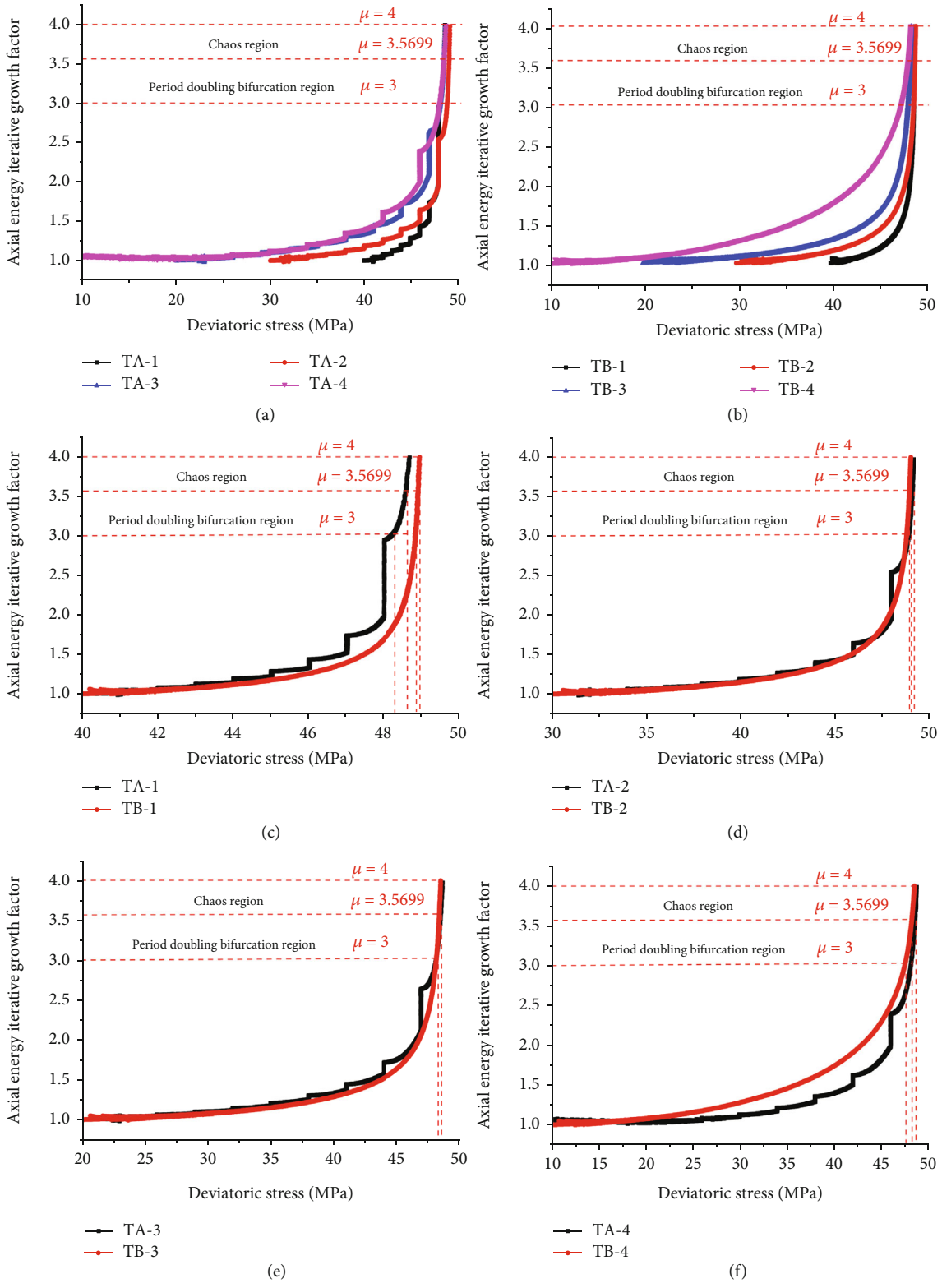

FIGURE 12: Relationship between μ value and deviatoric stress under triaxial unloading condition: (a) stress path 2, (b) stress path 3, and (c–f) comparison with two paths under the initial confining pressure of 10 MPa, 20 MPa, 30 MPa, and 40 MPa, respectively.

2.3358 MPa, 3.1282 MPa, and 5.2907 MPa, respectively, the system begin to appear chaotic regions.

From Figures 13(c)–13(f), under the same confining pressure of different paths: for the confining pressure of 10 MPa, path 2 reaches the period-doubling bifurcation region and chaotic region earlier than path 3. For the confining pressure of 20 MPa, path 3 reaches the period-doubling bifurcation region and chaotic region earlier than path 2.

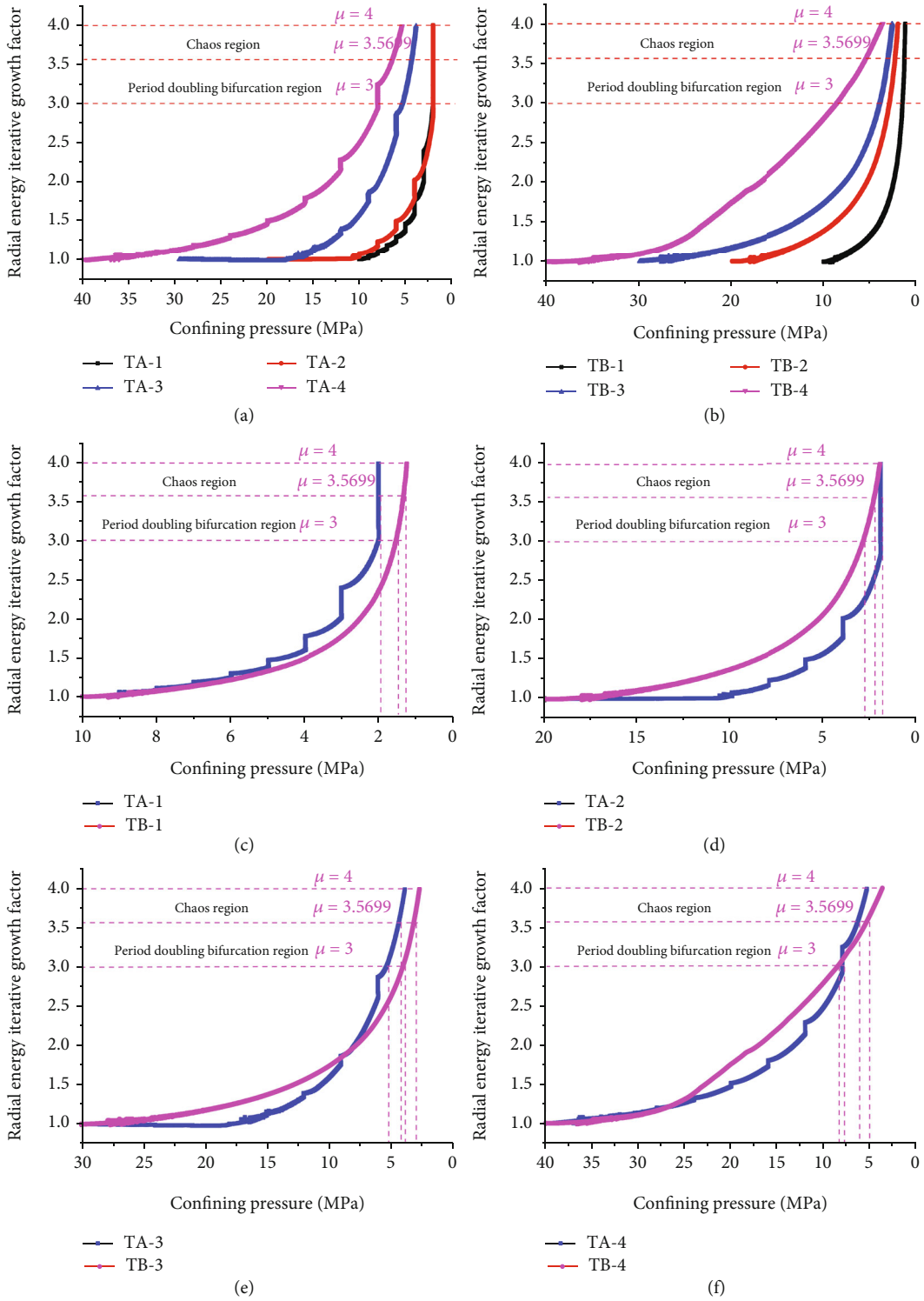

FIGURE 13: Relationship between μ value and confining pressure under triaxial unloading condition: (a) stress path 2, (b) stress path 3, and (c–f) comparison with two paths under the initial confining pressure of 10 MPa, 20 MPa, 30 MPa, and 40 MPa, respectively.

For the cases of 30 MPa and 40 MPa of the confining pressure, the curves have the same trend, with path 3 first advancing and then lagging behind path 2.

Figures 13(a) and 13(b) reveal that under different confining pressures on the same path: the larger the initial confining pressure, the earlier it reaches the period-doubling bifurcation region and chaotic region. The radial energy growth factor of multilevel unloading gradually slows down from a steep increase in the final stage, showing a slow-growth trend. The radial energy growth factor

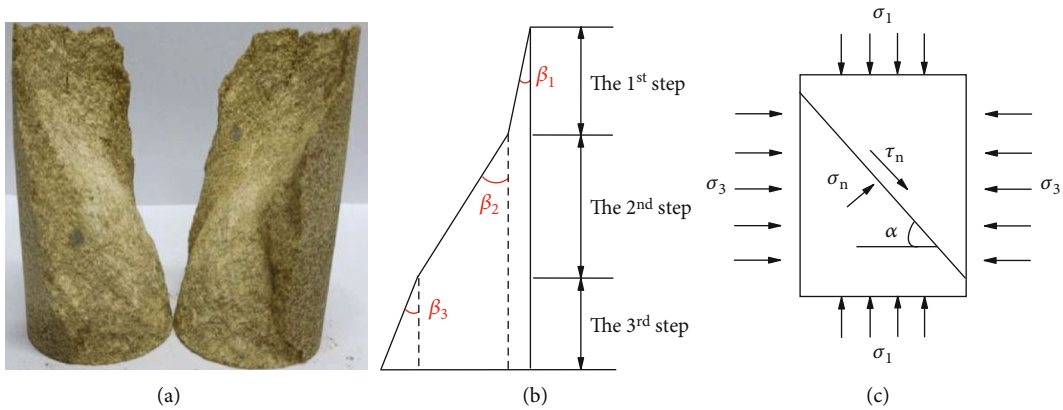

Figure 14: Characteristic of fracture morphology: (a) fracture picture, (b) three-step fracture model, and (c) stress analysis.

increases gradually when the confining pressure is low and the confining pressure is at 20 MPa and 30 MPa, there is a certain flat section with basically no increase, and the rock is in the linear elastic stage. The confining pressure is at 40 MPa; path 2 and path 3 grow basically synchronously in the early level, and there is no more flat section, and the growth rate of radial energy growth factor of path 3 is higher than that of path 2.

Under the unloading conditions, the mechanical conditions of the structural plane in the rock will change essentially; the original structural planes in the rock are subjected to tensile stress and open and expand rapidly. The samples are too late to carry out plastic deformation, and the strain cannot be effectively recovered. However, under higher confining pressures, the strain is recovered to a certain extent under multilevel unloading compared with conventional unloading, which makes the radial energy growth factor increase more slowly. During the unloading process of stress path 2, the radial energy growth factor enters the period-doubling bifurcation region at the 8th level, while the axial energy growth factor enters the period-doubling bifurcation region at the 9th and 10th levels. Through the comparison of Figures 12 and 13, the impact of confining pressure unloading on the radial energy growth factor is more sensitive than the axial energy growth factor. It is fully confirmed that the confining pressure has a certain inhibitory effect on energy, and the multilevel unloading makes the energy conversion more adequate and avoids the abrupt release of energy when the rock fails, which can decrease the possibility of rockburst and make the excavation unloading process safer.

5.3. Failure Modes and Constitutive Equations. Different failure modes may occur when the rock is stressed, producing the failure of the intact rock and failure along the structural plane. Assuming that the strength properties of both the intact rock and the structural plane satisfy the Mohr-Coulomb strength theory, the failure mode of the rock sample depends mainly on the angle between the external normal of the structural plane and the maximum principal stress. In this paper, the failure mode is explored in three steps according to the characteristics of confining pressure unloading under different paths, and the specific analysis can be summarized as follows: in the failure mode as shown in Figure 14, the failure of the second step in the middle of the sample is the compression shear failure with a complex stress state, and the failure of the first and third steps is the splitting failure caused by tensile stress.

Therefore, the first step can be approximately analyzed by the Mohr-Coulomb criterion (Figure 15). Considering the contact position between the sample and the experimental machine, an inclined plane with an angle of α is generated from the initial homogeneous medium under a certain stress state (σ_1, $\sigma_2 = \sigma_3$), as shown in Figure 14.

At this point, the stress on the inclined plane is:

$$\begin{aligned} \sigma_n &= \sigma_1 \cos^2\alpha + \sigma_3 \sin^2\alpha, \\ \tau_n &= \frac{(\sigma_1 - \sigma_3)\sin 2\alpha}{2}. \end{aligned} \tag{13}$$

Application of Mohr-Coulomb criterion on the inclined plane:

$$\begin{aligned} \tau_s &= \sigma_n \tan\varphi + C, \\ F &= \tau_s - \tau_n. \end{aligned} \tag{14}$$

As the shear fracture occurs, F is in the minimum state:

$$\frac{dF}{d\alpha} = 0. \tag{15}$$

The angle β of the shear fracture surface can be obtained:

$$\beta = 45^\circ + \frac{\varphi}{2}. \tag{16}$$

There are a large number of microcracks in rock. The deformation and fracture of rock is a comprehensive process of internal crack initiation, propagation, connection, and further formation of macrocracks under the action of external force. Figure 14(a) is the sample taken out to observe the fracture surface. It can be clearly seen that the samples are

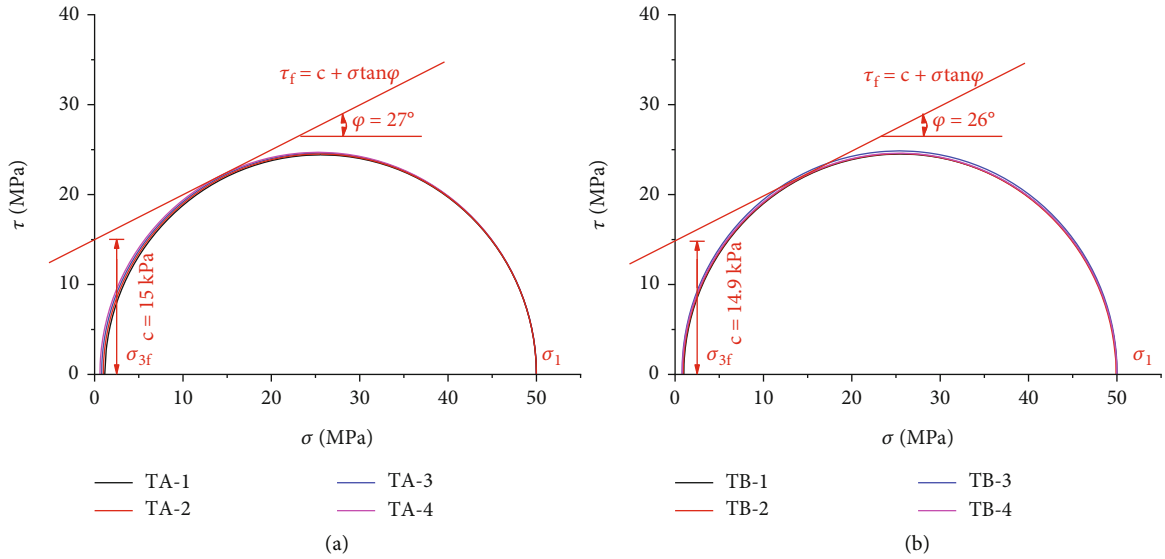

Figure 15: Mohr envelope of failure under stress paths 2 and 3: (a) stress path 2, (b) stress path 3.

Table 2: Statistics of triaxial compression tests.

Samples	Test scheme	Second step height (cm)	σ_{max} (MPa)	β_1 (°)	β_2 (°)	c (MPa)	φ (°)	Average value
TA-1	Stress path 2	6.0	50	29	63	11.60	36	$c_1 = 14.64$ $\varphi_1 = 27$
TA-2		5.8	50	26	60	13.59	30	
TA-3		5.7	50	23	56	16.28	22	
TA-4		5.5	50	20	55	17.08	20	
TB-1	Stress path 3	5.5	50	25	62	12.37	34	$c_2 = 14.96$ $\varphi_2 = 26$
TB-2		5.4	50	23	58	14.90	26	
TB-3		5.2	50	20	57	15.62	24	
TB-4		5.0	50	17	55	16.95	20	

subjected to shear failure along the inclined plane in terms of morphology.

Under the confining pressure action, a large amount of sandstone powder is found on the fracture surface, and the inclined fracture surface subjected to shear failure is staggered. On the surface of the uneven fracture, fine particles are exfoliated and show obvious traces of friction and dislocation.

At the end of the test, macroscopic shear failure occurs in the rock. The main shear plane is dispersed from one side to the other. It shows that the microcracks produced in the experiment mainly develop along the main failure surface under external interference and scarcely any aggregation of microcracks in other areas. These cracks have directivity and consistency peculiarity.

In view of the above analysis, the cohesion c and friction angle φ of the sample are calculated, respectively. The failure characteristics of each sample are counted and listed in Table 2 according to the pattern shown in Figure 14(b). Therefore, the average strength parameters of stress path 2 materials are $c_1 = 14.64$ MPa, $\varphi_1 = 27°$, and the average strength parameters of stress path 3 materials are $c_2 = 14.96$ MPa, $\varphi_2 = 26°$. It is close to Mohr's circle envelope $c_1 = 15$ MPa, $\varphi_1 = 27°$ and $c_2 = 14.9$ MPa, $\varphi_2 = 26°$. This also proves that there are tensile and shear fractures in the sample. The effects of tensile stress and shear stress are interdependent in the process.

6. Conclusions

In this study, multilevel and linear unloading triaxial compression tests with different confining pressures are separately carried out to systematically reveal the deformation, energy evolution, and fracture properties of sandstone samples under different stress paths. The research results can guide the prediction of rock instability mode and the selection of support and reinforcement measures. The following main conclusions can be drawn:

(1) The stress-strain curves have no obvious difference for path 2 and path 3. The higher the initial confining pressure, the smaller the axial strain of the initial unloading. During the unloading process, all kinds of strains remain basically unchanged at the early

level of unloading; the strain values change slightly in the middle level of unloading and change significantly at the late level of unloading

(2) Multilevel unloading has a suppressive effect on axial deformation and energy release. Especially in high confining pressure excavation unloading conditions, it is a safer unloading method that provides a certain buffer and recovery period for the rock and makes the excavation unloading process safer

(3) The radial energy growth factor is more sensitive than the axial energy growth factor under the unloading conditions, and the higher the initial confining pressure, the earlier the period-doubling bifurcation region and chaotic region are reached. The multilevel unloading makes the energy conversion more adequate, which reduces the sudden release of energy when the rock fails, decreasing the possibility of rockburst during excavation unloading

(4) The failure mode analysis shows that there are tensile and shear fractures in the sample. The effects of tensile stress and shear stress are interdependent in the process

Data Availability

The experimental data files and numerical simulation data files used to support the findings of this study are available from the corresponding author upon request.

Conflicts of Interest

The authors declare that they have no known competing financial interests or personal relationships that could have appeared to influence the work reported in this paper.

Acknowledgments

Reviewers and editors are thanked for their helpful suggestions and discussions. Financial support for this research is provided by the National Natural Science Foundation of China (grant nos. 52164001, 52064006, and 52004072), the Guizhou Provincial Science and Technology Foundation (grant nos. [2020]4Y044, [2021]292, [2020]2004, [2021]N404, and GCC[2022]005-1), Talents of Guizhou University (grant no. 201901), the Special Research Funds of Guizhou University (grant nos. 201903, 202011, and 202012), Guizhou University Cultivation Program (grant no. [2020] 1), and Higher Education Research Project of Guizhou University (grant no. GDGJYJ2021009).

References

[1] M. N. Bagde and V. Petros, "Fatigue properties of intact sandstone samples subjected to dynamic uniaxial cyclical loading," *International Journal of Rock Mechanics and Mining Science*, vol. 42, no. 2, pp. 237–250, 2005.

[2] X. S. Li, Q. H. Li, Y. J. Hu et al., "Study on three-dimensional dynamic stability of open-pit high slope under blasting vibration," *Lithosphere*, vol. 2021, no. Special 4, article 6426550, 2021.

[3] Y. Zhao, P. F. He, Y. F. Zhang, and C. L. Wang, "A new criterion for a toughness-dominated hydraulic fracture crossing a natural frictional interface," *Rock Mechanics and Rock Engineering*, vol. 52, no. 8, pp. 2617–2629, 2019.

[4] F. S. Zha, K. Huang, B. Kang et al., "Deterioration characteristic and constitutive model of red-bed argillaceous siltstone subjected to drying-wetting cycles," *Lithosphere*, vol. 2022, no. 1, article 8786210, 2022.

[5] L. L. Zheng, H. Y. He, Y. J. Zuo, H. Liu, X. R. Liu, and Q. Qiu, "Research on macro-micro failure mechanism of interbedded sandstone in the deep of Lannigou gold mine," *Lithosphere*, vol. 2022, no. Special 10, article 2998830, 2022.

[6] Y. Zhao, K. Zheng, C. L. Wang, J. Bi, and H. Zhang, "Investigation on model-I fracture toughness of sandstone with the structure of typical bedding inclination angles subjected to three-point bending," *Theoretical and Applied Fracture Mechanics*, vol. 119, article 103327, 2022.

[7] D. W. Yin, Y. S. Ding, N. Jiang, F. X. Li, J. C. Zhang, and H. H. Xu, "Mechanical properties and damage characteristics of coal samples under water immersion pressure," *Lithosphere*, vol. 2022, no. Special 10, article 1278783, 2022.

[8] B. Li, H. L. Zhang, Y. L. Luo, L. Liu, and T. Li, "Mine inflow prediction model based on unbiased Grey-Markov theory and its application," *Earth Science Informatics*, vol. 15, no. 2, pp. 855–862, 2022.

[9] S. B. Jin, X. Wang, Z. Wang, S. Y. Mo, F. S. Zhang, and J. Z. Tang, "Evaluation approach of rock brittleness index for fracturing acidizing based on energy evolution theory and damage constitutive relation," *Lithosphere*, vol. 2021, no. Special 4, article 2864940, 2021.

[10] Y. Zhao, J. Bi, and X. P. Zhou, "Effect of HTHP (high temperature and high pressure) of water on micro-characteristic and splitting tensile strength of gritstone," *Frontiers of Earth Science*, vol. 7, 2019.

[11] Y. Zhao, L. Zhang, W. Wang, J. Tang, H. Lin, and W. Wan, "Transient pulse test and morphological analysis of single rock fractures," *International Journal of Rock Mechanics and Mining Science*, vol. 91, pp. 139–154, 2017.

[12] B. Cerfontaine and F. Collin, "Cyclic and fatigue behaviour of rock materials: review, interpretation and research perspectives," *Rock Mechanics and Rock Engineering*, vol. 51, no. 2, pp. 391–414, 2018.

[13] L. R. Alejano and E. Alonso, "Considerations of the dilatancy angle in rocks and rock masses," *International Journal of Rock Mechanics and Mining Science*, vol. 42, no. 4, pp. 481–507, 2005.

[14] V. Hajiabdolmajid, P. K. Kaiser, and C. D. Martin, "Modelling brittle failure of rock," *International Journal of Rock Mechanics and Mining Science*, vol. 39, pp. 731–741, 2002.

[15] Z. Y. Liu, J. F. Xue, and J. Z. Ye, "The effects of unloading on drained cyclic behaviour of Sydney sand," *Acta Geotechnica*, vol. 16, no. 9, pp. 2791–2804, 2021.

[16] W. T. Tun, T. Sato, H. Saito, and Y. J. Kohgo, "Mechanical properties and stress–dilatancy relationships of unsaturated soil under various cyclic loading conditions," *Acta Geotechnica*, vol. 15, no. 7, pp. 1799–1813, 2020.

[17] Z. Y. Song, H. Konietzky, Y. F. Wu, and X. Cai, "Mechanical and microseismic characteristics of sandstones subject to moderate low-frequency differential cyclic loading (DCL) followed by monotonic loading up to failure," *Acta Geotechnica*, 2022.

[18] P. F. Liu, X. F. Liu, G. D. Tian, F. Gan, and J. Bi, "Effect of thermal cycling and hydro-thermal cycling on physical and mechanical properties of sandstone," *Energy Science & Engineering*, vol. 8, no. 3, pp. 718–730, 2019.

[19] Y. Rui, J. K. Lv, Z. Bo, and D. P. Ma, "Rock unloading failure precursor based on acoustic emission parametric fractal characteristics," *Lithosphere*, vol. 2022, no. Special 11, article 8221614, 2022.

[20] J. T. Hong and M. Xu, "DEM study on the undrained mechanical behavior of gassy sand," *Acta Geotechnica*, vol. 15, no. 8, pp. 2179–2193, 2020.

[21] L. M. Zhang, Y. Cong, F. Z. Meng, Z. Q. Wang, P. Zhang, and S. Gao, "Energy evolution analysis and failure criteria for rock under different stress paths," *Acta Geotechnica*, vol. 16, no. 2, pp. 569–580, 2021.

[22] D. Huang and Y. Li, "Conversion of strain energy in triaxial unloading tests on marble," *International Journal of Rock Mechanics and Mining Science*, vol. 66, pp. 160–168, 2014.

[23] Q. S. Liu, Z. C. Qian, and Z. J. Wu, "Micro/macro physical and mechanical variation of red sandstone subjected to cyclic heating and cooling: an experimental study," *Bulletin of Engineering Geology and the Environment*, vol. 78, no. 3, pp. 1485–1499, 2017.

[24] Y. Zhao, C. L. Wang, L. Ning, H. F. Zhao, and J. Bi, "Pore and fracture development in coal under stress conditions based on nuclear magnetic resonance and fractal theory," *Fuel*, vol. 309, article 122112, 2022.

[25] F. Q. Gong, J. Y. Yan, S. Luo, and X. B. Li, "Investigation on the linear energy storage and dissipation laws of rock materials under uniaxial compression," *Rock Mechanics and Rock Engineering*, vol. 52, no. 11, pp. 4237–4255, 2019.

[26] X. Lei, F. Q. Gong, and S. Luo, "Effects of pre-existing single crack angle on mechanical behaviors and energy storage characteristics of red sandstone under uniaxial compression," *Theoretical and Applied Fracture Mechanics*, vol. 113, article 102933, 2021.

[27] K. Peng, J. Q. Zhou, Q. L. Zou, and F. Z. Yan, "Deformation characteristics of sandstones during cyclic loading and unloading with varying lower limits of stress under different confining pressures," *International Journal of Fracture*, vol. 127, pp. 82–100, 2019.

[28] K. Fuenkajorn and D. Phueakphum, "Effects of cyclic loading on mechanical properties of Maha Sarakham salt," *Engineering Geology*, vol. 112, no. 1–4, pp. 43–52, 2010.

[29] Y. P. Liang, Q. M. Li, Y. L. Gu, and Q. L. Zou, "Mechanical and acoustic emission characteristics of rock: effect of loading and unloading confining pressure at the postpeak stage," *Journal of Natural Gas Science and Engineering*, vol. 44, pp. 54–64, 2017.

[30] D. Y. Li, Z. Sun, T. Xie, X. B. Li, and P. G. Ranjith, "Energy evolution characteristics of hard rock during triaxial failure with different loading and unloading paths," *Engineering Geology*, vol. 228, pp. 270–281, 2017.

[31] R. X. Shen, T. Q. Chen, T. X. Li et al., "Study on the effect of the lower limit of cyclic stress on the mechanical properties and acoustic emission of sandstone under cyclic loading and unloading," *Theoretical and Applied Fracture Mechanics*, vol. 108, article 102661, 2020.

[32] P. Z. Zhuang, H. S. Yu, S. J. Mooney, and P. Q. Mo, "Loading and unloading of a thick-walled cylinder of critical-state soils: large strain analysis with applications," *Acta Geotechnica*, vol. 16, no. 1, pp. 237–261, 2021.

[33] C. D. Martin and N. A. Chandler, "The progressive fracture of Lac du Bonnet granite," *International Journal of Rock Mechanics and Mining Science*, vol. 31, no. 6, pp. 643–659, 1994.

[34] H. R. Renani and C. D. Martin, "Cohesion degradation and friction mobilization in brittle failure of rocks," *International Journal of Rock Mechanics and Mining Science*, vol. 106, pp. 1–13, 2018.

[35] S. F. Wang, L. Q. Huang, and X. B. Li, "Analysis of rockburst triggered by hard rock fragmentation using a conical pick under high uniaxial stress," *Tunnelling and Underground Space Technology*, vol. 96, article 103195, 2020.

[36] Y. Zhao, J. Bi, C. L. Wang, and P. F. Liu, "Effect of unloading rate on the mechanical behavior and fracture characteristics of sandstones under complex triaxial stress conditions," *Rock Mechanics and Rock Engineering*, vol. 54, no. 9, pp. 4851–4866, 2021.

[37] Y. Wang, W. K. Feng, and C. H. Li, "On anisotropic fracture and energy evolution of marble subjected to triaxial fatigue cyclic-confining pressure unloading conditions," *International Journal of Fatigue*, vol. 134, article 105524, 2020.

[38] S. F. Wang, X. B. Li, J. R. Yao et al., "Experimental investigation of rock breakage by a conical pick and its application to non-explosive mechanized mining in deep hard rock," *International Journal of Rock Mechanics and Mining Sciences*, vol. 122, article 104063, 2019.

[39] X. T. Feng, H. Xu, C. X. Yang, X. W. Zhang, and Y. H. Gao, "Influence of loading and unloading stress paths on the deformation and failure features of Jinping marble under true triaxial compression," *Rock Mechanics and Rock Engineering*, vol. 53, no. 7, pp. 3287–3301, 2020.

[40] Q. L. Ding, F. Ju, X. B. Mao, D. Ma, B. Y. Yu, and S. B. Song, "Experimental investigation of the mechanical behavior in unloading conditions of sandstone after high-temperature treatment," *Rock Mechanics and Rock Engineering*, vol. 49, no. 7, pp. 2641–2653, 2016.

[41] Y. Zhao, S. Dang, J. Bi, C. L. Wang, and F. Gan, "Influence of complex stress path on energy characteristics of sandstones under triaxial cyclic unloading condition," *International Journal of Geomechanics*, vol. 22, no. 6, article 04022076, 2022.

[42] Z. Z. Zhang, M. Deng, J. B. Bai, X. Y. Yu, Q. H. Wu, and L. S. Jiang, "Strain energy evolution and conversion under triaxial unloading confining pressure tests due to gob-side entry retained," *International Journal of Rock Mechanics and Mining Science*, vol. 126, article 104184, 2020.

[43] Y. Z. Liu, P. Cao, L. W. He, and Q. B. Lin, "Failure behaviour of sandstone with a preexisting joint under leveled excavation," *Advances in Civil Engineering*, vol. 2020, Article ID 8884736, 11 pages, 2020.

[44] L. F. Fan, J. W. Gao, X. L. Du, and Z. J. Wu, "Spatial gradient distributions of thermal shock-induced damage to granite," *Journal of Rock Mechanics and Geotechnical Engineering*, vol. 12, no. 5, pp. 917–926, 2020.

[45] Z. Z. Zhang and F. Gao, "Research on nonlinear characteristics of rock energy evolution under uniaxial compression," *Journal of Rock Mechanics and Geotechnical Engineering*, vol. 31, no. 6, pp. 1198–1207, 2012.

[46] X. P. Zhou, Y. Niu, H. Cheng, and F. Berto, "Cracking behaviors and chaotic characteristics of sandstone with unfilled and

filled dentate flaw," *Theoretical and Applied Fracture Mechanics*, vol. 112, article 102876, 2021.

[47] B. Li, H. L. Zhang, J. Long et al., "Migration mechanism of pollutants in karst groundwater system of tailings impoundment and management control effect analysis: gold mine tailing impoundment case," *Journal of Cleaner Production*, vol. 350, article 131434, 2022.

[48] G. Walton and M. S. Diederichs, "A new model for the dilation of brittle rocks based on laboratory compression test data with separate treatment of dilatancy mobilization and decay," *Geotechnical and Geological Engineering*, vol. 33, no. 3, pp. 661–679, 2015.

[49] M. Cudny and A. Truty, "Refinement of the hardening soil model within the small strain range," *Acta Geotechnica*, vol. 15, no. 8, pp. 2031–2051, 2020.

[50] F. Wu, H. Zhang, Q. L. Zou, C. B. Li, J. Chen, and R. B. Gao, "Viscoelastic-plastic damage creep model for salt rock based on fractional derivative theory," *Mechanics of Materials*, vol. 150, article 103600, 2020.

[51] Q. Feng, J. C. Jin, S. Zhang, W. W. Liu, X. X. Yang, and W. T. Li, "Study on a damage model and uniaxial compression simulation method of frozen–thawed rock," *Rock Mechanics and Rock Engineering*, vol. 55, no. 1, pp. 187–211, 2021.

[52] Y. Zhao, Y. Wang, W. Wang, W. Wan, and J. Tang, "Modeling of non-linear rheological behavior of hard rock using triaxial rheological experiment," *International Journal of Rock Mechanics and Mining Science*, vol. 93, pp. 66–75, 2017.

[53] M. M. Kou, J. Bi, B. H. Yuan, and Y. T. Wang, "Peridynamic analysis of dynamic fracture behaviors in FGMs with different gradient directions," *Structural Engineering and Mechanics*, vol. 75, no. 3, pp. 339–356, 2020.

[54] E. Eberhardt, D. Stead, and B. Stimpson, "Quantifying progressive pre-peak brittle fracture damage in rock during uniaxial compression," *International Journal of Rock Mechanics and Mining Science*, vol. 36, no. 3, pp. 361–380, 1999.

[55] C. D. Martin, R. Christiansson, and J. Soederhaell, *Rock stability considerations for siting and constructing a KBS-3 repository. Based on experiences from Aespoe HRL, AECL's URL, tunnelling and mining (No. SKB-TR–01-38)*, vol. 12, Swedish Nuclear Fuel and Waste Management Co., 2001.